LAWRENCE
LIVERMORE
NATIONAL
LABORATORY

LLNL-JRNL-823826

The Influence of LiH and TiH2 on Hydrogen Storage in MgB2 II. XPS Study of Surface and Near-surface Phenomena

J. L. Snider, T. M. Mattox, Y. S. Liu, L. Wan, P. Wijeratne, M. D. Allendorf, V. Stavila, B. C. Wood, L. E. Klebanoff

June 24, 2021

International Journal of Hydrogen Energy

Disclaimer

The Influence of LiH and TiH_2 on Hydrogen Storage in MgB_2

II. XPS Study of Surface and Near-surface Phenomena

J.L. Snider[1], T.M. Mattox[2], Y.-S. Liu[3], L.F. Wan[4], P. Wijeratne[1], M.D. Allendorf[1], V. Stavila[1], B.C. Wood[4] and L.E. Klebanoff[1]*

[1]*Sandia National Laboratories, Livermore, CA 94551-0969, USA*
[2]*Molecular Foundry, Lawrence Berkeley National Laboratory, Berkeley, CA 94720 USA*
[3]*Advanced Light Source, Lawrence Berkeley National Laboratory, Berkeley, CA 94720 USA*
[4]*Lawrence Livermore National Laboratory, Livermore, CA 94551, USA*

**Corresponding Author: L.E. Klebanoff, Tel: 925-294-3471; email: lekleba@sandia.gov*

Dedication: This study is dedicated to Dr. David A. Shirley, formerly Professor of Chemistry at the University of California-Berkeley as well as Director of the Lawrence Berkeley National Laboratory. Dave passed away as this manuscript was nearing completion. The world has lost a pioneer in the use of ionizing radiation and electrons to probe the nature of matter, and one of us (Lennie Klebanoff) lost a trusted mentor and Ph.D. thesis advisor.

Abstract

$Mg(BH_4)_2$ is a promising solid-state hydrogen storage material, releasing 14.9 wt.% hydrogen upon conversion to MgB_2. The rehydrogenation of MgB_2 is particularly challenging, requiring prolonged exposure to high pressures of hydrogen at high temperature. Here we report an XPS study probing the influence of LiH and TiH_2 on the hydrogen storage properties of MgB_2 in the surface and near-surface regions, as a complementary investigation to a preceding study of the bulk properties. Surface and near-surface properties are important considerations for nanoscale and bulk hydrogen storage materials. If there are reactions occurring at the surface that modify the chemical composition in the near-surface region, species diffusion can alter the chemical composition even deep into the bulk of the material. For LiH/MgB_2, metastable LiH-B and LiH-Mg species are produced that are more reactive than Bulk MgB_2. With prolonged glovebox storage, the LiH/MgB_2 material shows increased reactivity towards O and C and enriched levels of Li and B in the near-surface region. In addition, Li induces the growth of Li_2CO_3 in the surface and near surface regions. Exposing LiH/MgB_2 to hydrogen at 700 bar and 280 ºC for 24 hours produces borohydride at a temperature 100 ºC below the threshold for bulk MgB_2 hydrogenation. In a specifically surface process with macroscopic implications, the hydrogenation conditions also cause Li_2CO_3 to react with boron hydroxide in the sample to form a Li-deficient glassy lithium borate melt at the interfaces of the particles, bonding them together. Subsequent heating to 380 ºC dehydrogenates the borohydride and eliminates the Li-deficient glassy lithium borate. The LiH/MgB_2 material is not reversible because desorption does not lead back to LiH/MgB_2, but rather to elemental B and Mg metal in the near-surface region. In contrast to LiH, TiH_2 does not react with MgB_2, despite the favorable thermodynamics for destabilization

via TiB_2 formation. Furthermore, high pressure hydrogenation yields only unreacted TiH_2 and MgB_2 in the surface and near-surface regions. Thus, added TiH_2 provides no benefit to MgB_2 hydrogenation, in agreement with the findings of the preceding bulk study.

Keywords: Hydrogen Storage, Magnesium Diboride, Additive, Lithium Hydride, XPS

Introduction

Surface and near-surface properties are important for nanoscale and bulk hydrogen storage materials. For nanoscale materials, with particle diameter of ~ 50 nm, 49 percent of the atoms lie within 10 nm of the surface. This percentage increases to 100% for 20 nm diameter particles. Even for bulk powder materials, for which the typical particle size is ~ 500 nm diameter [1], 11% of the atoms lie within 10 nm of the surface, which is a non-trivial amount. If there are reactions occurring at the surface that modify the chemical composition, species diffusion can alter the chemical composition even deep into the bulk of the material. The nature of the surface chemistry can also have a practical impact on how the particles adhere to each other and thus affect material packing into practical hydrogen storage tanks. During bulk hydrogenation, hydrogen must pass from the gas phase through the near-surface region to reach the bulk material [2]. Similarly, during dehydrogenation, hydrogen must pass from the bulk through the near-surface region to reach the gas phase. Thus, understanding the nature of the chemical processes occurring within 10 nm of a material's surface is important for a complete understanding of hydrogen storage materials chemistry. This has been recognized by others, where the modern techniques of surface science, especially x-ray photoelectron spectroscopy (XPS), have been brought to bear on such diverse hydrogen storage issues as surface segregation [2], catalytic additives [3, 4], carbon nanotube decoration [5], core shell structuring [6], and surface contamination [7, 8].

We seek to understand the influence of LiH and TiH_2 on the hydrogenation of MgB_2, with the initial goal of disrupting the stable B-B ring in MgB_2 that is believed to hinder facile hydrogenation to borohydride [1]. This investigation complements prior studies [9,10] which reported that LiH reduces the hydrogen desorption temperature of $Mg(BH_4)_2$. We are unaware of studies involving the combination of TiH_2 and MgB_2. TiH_2 is predicted to produce strong destabilization (via formation of TiB_2) when combined with $LiBH_4$ [11, 12], suggesting TiH_2 could be a source of potent B-B ring disruption in MgB_2.

The preceding companion study (I) [13] examined the hydrogenation/dehydrogenation phenomena occurring in the bulk of LiH/MgB_2 and TiH_2/MgB_2. In this study (II), we investigate the surface phenomena occurring to a depth of ~ 10 nm when LiH and TiH_2 are introduced to MgB_2, exposed to hydrogen at high pressure and elevated temperatures, and subsequently heated to desorb hydrogen. Here we show that metastable LiH-MgB_2 species are initially formed that evolve over time, and significantly increase the overall reactivity of the system, leading to

borohydride production 100 ºC below the threshold for bulk MgB_2 hydrogenation. In contrast to LiH, TiH_2 does not react with MgB_2, and provides no benefit to MgB_2 hydrogenation.

Experimental Methods

Sample preparation and handling were conducted at Sandia National Laboratories (SNL) in an Ar-filled glove-box equipped with a recirculation system that keeps H_2O and O_2 concentrations below 0.1 ppm. Experimental sample preparation details are provided in the Supporting Information (SI) associated with the companion study (I) [13].

Five primary substances used in the study were:

1. Bulk MgB_2: MgB_2 ball-milled for 2 hours.
2. [Low LiH/MgB_2]: LiH added to MgB_2 and ball-milled for one hour. The mole fraction of LiH to MgB_2 was 0.22.
3. [High LiH/MgB_2]: LiH added to MgB_2 and ball-milled for one hour. The mole fraction of LiH to MgB_2 was 0.43.
4. [Low TiH_2/MgB_2]: TiH_2 added to MgB_2 and ball-milled for one hour. The mole fraction of TiH_2 to MgB_2 was 0.24.
5. [High TiH_2/MgB_2]: TiH_2 added to MgB_2 and ball-milled for one hour. The mole fraction of TiH_2 to MgB_2 was 0.44.

Several other commercial chemicals were used as spectroscopic standards, including B_2O_3, MgO, Mg metal, LiB_2, LiOH and $LiBH_4$ with details given in the SI.

XPS was used to probe the chemistry in the surface and near-surface regions of these materials. The XPS measurements were conducted at Lawrence Berkeley National Laboratory's Molecular Foundry. The K-Alpha Plus instrument utilized a monochromatic Al K_α x-ray source with a 400-micron spot size and a low-energy electron flood source for charge neutralization. Small amounts (~ 10 mg) of powder samples were pressed onto silver tape within an argon glovebox and loaded into the instrument using an air-free vacuum transfer holder. For all samples, the C 1s XPS peak of adventitious C contamination was used as an internal binding energy reference standard at 284.48 eV [1]. As needed, depth profiling was performed using a dual monoatomic and gas cluster argon-ion source, with samples etched for various times at 2000 eV ion energy using low current. Unless specified otherwise, all reported XPS spectra are for "zero-etch" conditions for which no ion-milling occurred. All of the XPS data were analyzed using Casa XPS software which uses Scofield cross section input.

High-pressure (HP) hydrogenation experiments at SNL were performed at 700 bar H_2 and 280 °C in a high-pressure reactor with a Newport Scientific compressor and a vessel made from 316L stainless steel. Samples were loaded inside the argon glovebox. Hydrogen desorption from hydrogenated samples was studied using the PCTPro 2000 (Setaram, Inc.) at SNL. Hydrogen

capacity data are presented as weight percent of H desorbed with respect to the total sample weight: wt.% desorbed = [mass H desorbed]/[(mass H desorbed + mass MgB_2 original sample)] x 100. Desorption measurements into static vacuum were conducted using a temperature ramp of 3 °C/min. More details are provided in the SI of (I) [13].

The depth sensitivity for XPS depends on the kinetic energy (KE) of the photoelectron relative to the sample Fermi Level, as described previously [1]. The inelastic mean free path (IMFP) λ (nm) of the photoelectrons is calculated using the equation derived by Seah and Dench for inorganic compounds [14]. From λ (nm), one can calculate the depth D whose photoelectric signal (I) comprises 10% of the photoelectron contribution from the surface layer (I_o). We call D the "depth sensitivity" since layers above the depth D contribute 90% of the total photoelectric signal. Since $I/I_o = e^{-[D/\lambda]}$, using a value of $I/I_o = 0.1$ and calculated values of λ (nm), we can estimate values of D for the core-level XPS peaks measured in our study. Table I provides calculated values of λ (nm) and D (nm) for the XPS investigations.

Table 1: Depth Sensitivity of the XPS Core-level Peaks

XPS Peak	Core-level Binding Energy (eV)	Photoelectron Kinetic Energy (eV)	IMFP, λ (nm)	Depth Sensitivity, D (nm)
Mg 2p	50	1437	3.6	8.4
Li 1s	56	1443	3.6	8.4
B 1s	187	1300	3.5	8.0
C 1s	284.5	1202.5	3.3	7.7
Ti $2p_{3/2}$	455	1032	3.1	7.1
O 1s	531	956	3.0	7.1

As indicated in Table 1, all of the core-level XPS data have at least 90% of their contribution from within the topmost 8.4 nm of the sample surface.

Results and Discussion

Our analysis of the XPS results indicates that TiH_2 has no effect on the surface chemistry or hydrogen storage properties of MgB_2, whereas LiH has a dramatic influence on surface and near-surface stability, composition, and reactivity. These are discussed in more detail below beginning with the "as prepared" materials, then moving to the materials produced by high-pressure hydrogenation of LiH/MgB_2, and finally the nature of hydrogen desorption from the hydrogenated LiH/MgB_2 materials.

TiH_2/MgB_2: Characterization of the "As-prepared" Materials

The influence of TiH_2 on the hydrogen storage chemistry of MgB_2 was considered first, with the results showing no influence observed with the TiH_2 additive. Thermodynamically, TiB_2 formation is expected when TiH_2 and MgB_2 are combined, since the reaction: $TiH_2 + MgB_2 \rightarrow TiB_2 + MgH_2$ has a favorable ΔH_{rxn} of -118.38 kJ/mole [15]. Fig. 1 presents XPS spectra for the "as-prepared" [Low TiH_2/MgB_2] and [High TiH_2/MgB_2], as well as for these samples exposed to HP hydrogen for 24 hours at 700 bar and 280 °C, producing samples [Low TiH_2/MgB_2 HP] and [High TiH_2/MgB_2 HP], respectively. The data indicate no significant changes in the B (Fig. 1(a)) or Mg (Fig. 1(b)) lineshapes that would suggest reaction, either during original ball-milling or during HP hydrogenation. This finding is in agreement with the bulk data from x-ray diffraction (XRD), Fourier Transform Infra-red (FTIR) spectroscopy, nuclear magnetic resonance (NMR) and x-ray absorption spectroscopy (XAS) that were reported in (I) [13]. The B 1s XPS peak at 191.8 eV is boron hydroxide, as opposed to the hard oxide B_2O_3, as discussed previously [16] and shown in Fig. 1(a). The Ti $2p_{3/2,1/2}$ spectra in Fig. 1(c) show that the TiH_2 additive initially has a significant oxide component that gets reduced with hydrogen exposure.

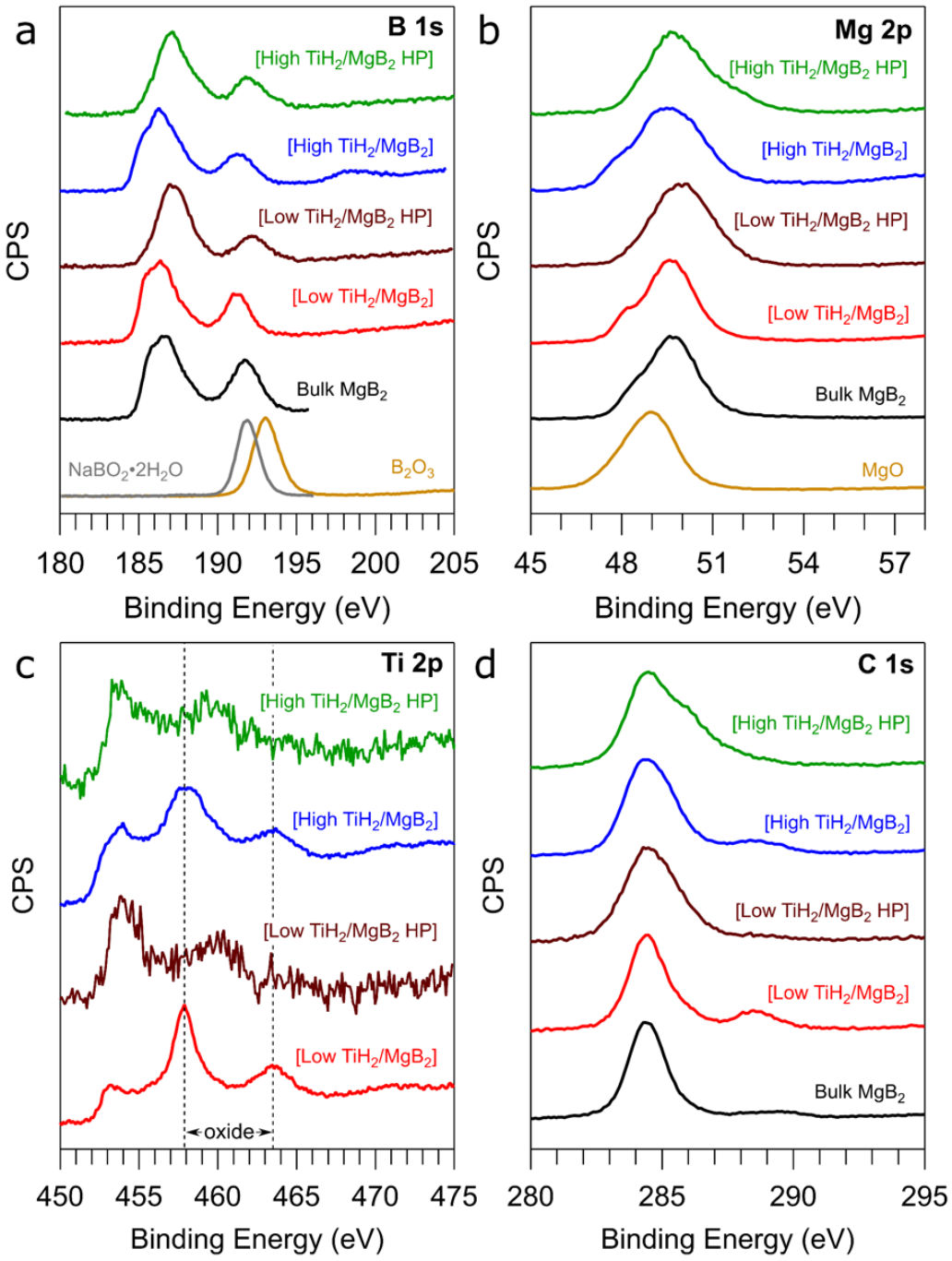

Fig. 1: XPS data for "as-prepared" [Low TiH_2/MgB_2] and [High TiH_2/MgB_2], as well as for these samples exposed to HP hydrogen for 24 hours at 700 bar and 280 °C, producing samples [Low TiH_2/MgB_2 HP] and [High TiH_2/MgB_2 HP], respectively. Core-level XPS data are measured for the (a) B 1s, (b) Mg 2p, (c) Ti $2p_{3/2,1/2}$, with dotted lines indicating oxide peaks measured from a TiO_2 standard powder and (d) C 1s regions. These are zero-etch spectra, collected without prior ion-etching of the material. Panel (a) includes B 1s data from B_2O_3 and $NaBO_2 \cdot 2H_2O$ standard powders.

The C 1s main peak at 284.48 eV is characteristic of the aliphatic (C-C) portion of hydrocarbon molecules. The weak feature that appears in the [Low TiH_2/MgB_2] and [High TiH_2/MgB_2] C 1s data at 289.5 eV is due to surface carbonate (CO_3^{2-}). Indeed, Aswal and co-workers have reported [17] that when the MgB_2 is immersed in water for 72 hours, some of the adventitious C on the sample is converted to carbonate with a binding energy of 289.1 eV, referenced to our C 1s aliphatic binding energy standard. Fig. 1(d) shows that the HP hydrogenation process removes surface carbonate, presumably due to a reduction process followed by desorption of CO_2.

Although the [Low TiH_2/MgB_2] and [High TiH_2/MgB_2] samples show no evidence for additive reaction, complex formation, or more facile hydrogenation, they do serve as useful control samples since they were processed identically to the LiH/MgB_2 samples with regard to synthesis, handling, characterization, hydrogenation and desorption. The remainder of this study will focus on LiH/MgB_2, with XPS results presented for the TiH_2/MgB_2 control samples as needed.

LiH/MgB_2: Characterization of the As-prepared Materials

In contrast to TiH_2, rather dramatic changes occur when LiH is added to MgB_2. In particular, evidence is found for a dynamic and complex LiH/MgB_2 near-surface environment, with LiH-induced changes in the local electronic structure at B and Mg, with time-dependent changes in near-surface composition and surface-induced reactions that have consequences for the bulk properties of the material.

Local Electronic Structure:

LiH was found to modify the local electronic structure at the B and Mg atoms in the MgB_2 host. XPS data for the as-prepared [Low LiH/MgB_2] and [High LiH/MgB_2] samples are shown in Fig. 2. There are LiH-induced changes in both the B 1s and Mg 2p spectra. The bulk experiments reported in (I) [13] showed that LiH remain undissociated in the as prepared materials, so we start our discussion from that position.

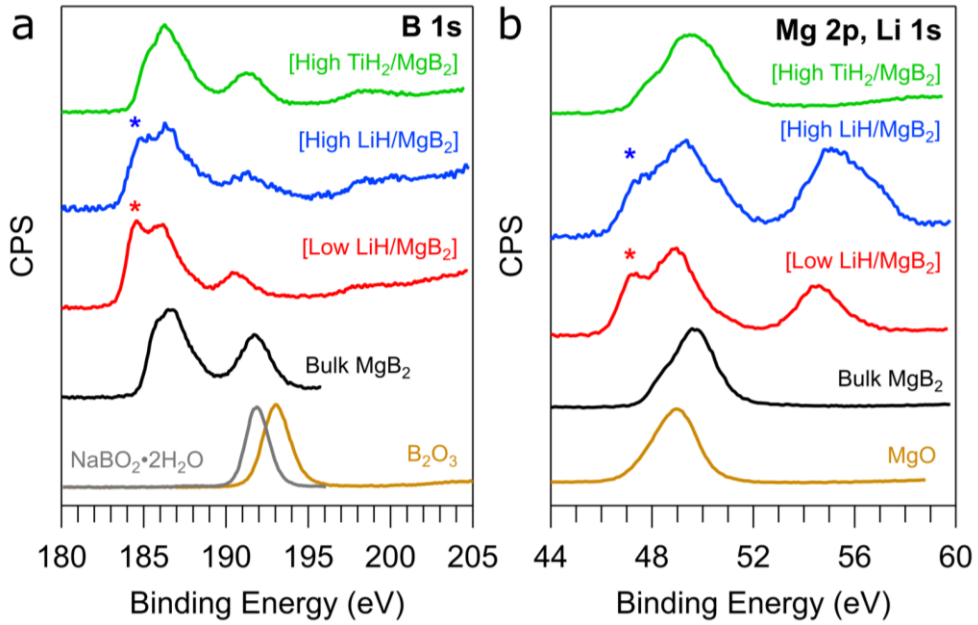

Fig. 2: XPS spectra for the [Low LiH/MgB_2] and [High LiH/MgB_2] samples. (a) the B 1s level with asterisk marking the LiH-induced feature and (b) the combined Mg 2p and Li 1s levels with an asterisk marking the LiH-induced feature at the Mg 2p peak. Spectra are also presented for standard powders $NaBO_2 \cdot 2H_2O$, B_2O_3 and MgO along with spectra collected for Bulk MgB_2 and [High TiH_2/MgB_2] for comparison.

Starting with the B 1s spectra in Fig. 2(a), we see that for both [Low LiH/MgB_2] and [High LiH/MgB_2] there is a LiH-induced feature (marked with an asterisk) located at lower binding energy (185.0 eV) from the main boride-like feature at 186.2 eV. This B feature, appearing ~ 1.2 eV to lower binding energy, cannot be attributed to B-O contamination, which produces B peaks at higher binding energy relative to the boride peak. Also, this feature appears only for the Li-containing samples and not the [High TiH_2/MgB_2] control sample, arguing against it being attributable to an artifact (e.g., carbon contamination) during ball milling.

Fig. 2(b) shows that there is a LiH-induced feature (marked with an asterisk) at the Mg 2p peak as well for both [Low LiH/MgB_2] and [High LiH/MgB_2]. This feature is shifted 1.6 eV to lower binding energy than the Mg 2p peak for pure MgB_2. The leading-edge feature does not correspond in position to MgO. Also, it only appears for the Li-containing samples, and not for the Ti-containing control samples.

The Li 1s feature is located at ~ 55 eV in Fig. 2(b). There is no evidence in any of the Li 1s spectra of a plasmon loss feature which would be located 7.5 eV to higher binding energy [18], thus metallic Li can be excluded. The integrated intensity of the Li 1s feature for the [High LiH/MgB_2] sample is 1.9 times larger than for the [Low LiH/MgB_2] sample, consistent with the

sample preparation. The [High LiH/MgB_2] has a wider distribution of Li 1s binding energies, reflecting multiple LiH-containing species being present.

The appearance of the LiH-induced feature at 185.0 eV in Fig. 2(a) suggests some B species may be polarized more negatively than the B in MgB_2. From the ab initio molecular dynamics (AIMD) simulations discussed in (I), it is observed that the introduction of LiH disturbs the electronic states of the B plane such that some B atoms are slightly more or less negatively charged than the B atoms in pristine MgB_2 due to local variations in B-B bond length and interactions with H. The results for the AIMD local charge analysis are shown in Fig. 3. Elongated B-B bonds (leading to an expanded B-B hexagonal ring) at the LiH/MgB_2 interface may lead to more negatively charged B atom, such as the B atoms showing the -1.02e and -1.44e Bader charges in Fig. 3, compared to the pristine MgB_2 material (-0.80e). Once the B atoms start to interact with H at the interface, they can become less negatively charged and, in some cases, can slip their charges to become slightly positively charged. Note that these charges on individual atoms are dynamically changing and the charges highlighted in Fig. 3 represent instantaneous charge on selected atoms during the AIMD simulations.

Overall, this fluctuation of the B charge states may contribute to the LiH-induced XPS feature observed in Fig. 2(a). This observed modification to the B electronic structure due to LiH addition is also consistent with the NMR finding in (I) [13] that the boride-like ^{11}B chemical shifts for both [Low LiH/MgB_2] and [High LiH/MgB_2] are shifted markedly from that observed for pure MgB_2 [13]. Analogously, the appearance of the LiH-induced feature at lower binding energy for Mg 2p suggests some Mg species become less positively charged than the Mg in pure MgB_2. This is observed in the simulation where the Mg atoms at the interface are positively charged by ~ + 1.56e compared to +1.62e in the pristine MgB_2 lattice (Fig. 3). A full account of the AIMD study of LiH/MgB_2 will be the subject of a future publication.

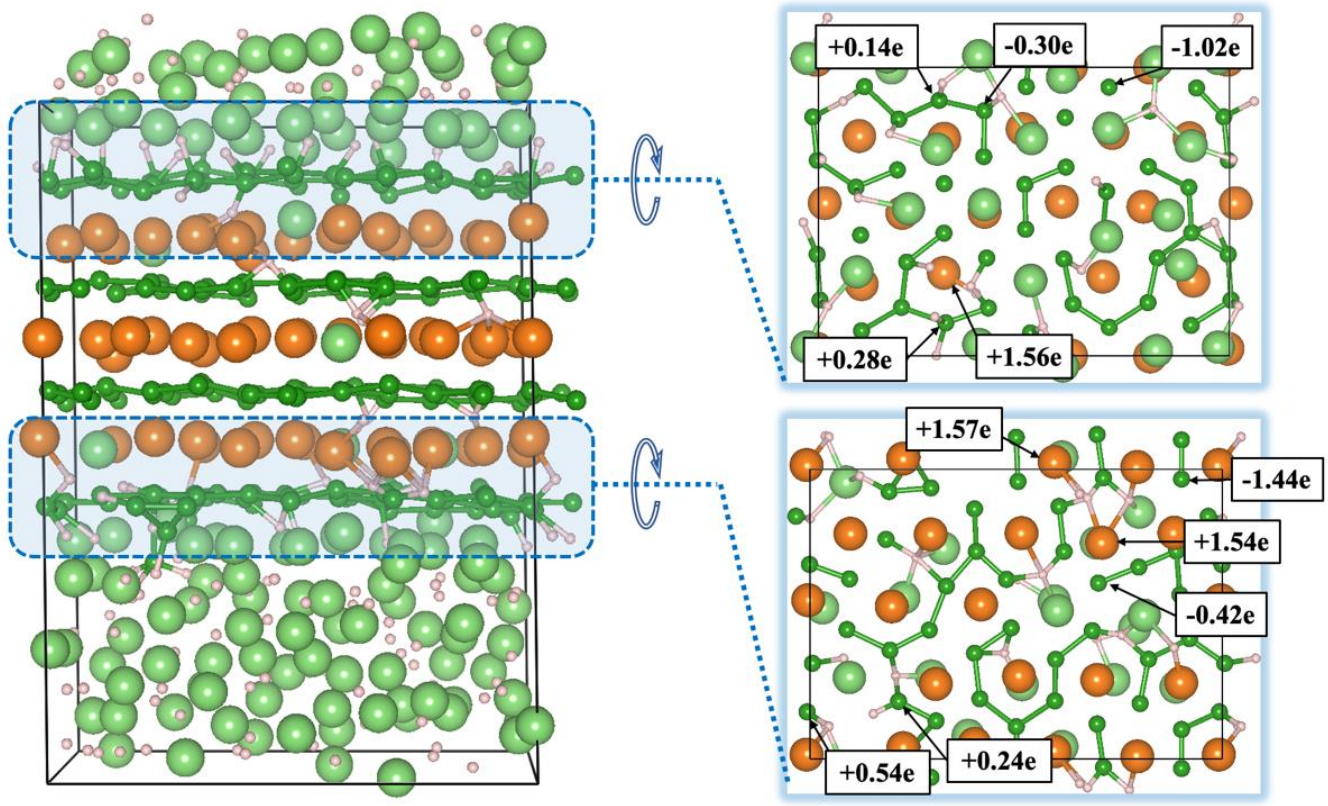

Fig. 3: Snapshot of the LiH/MgB_2 interfacial structure (left), comprised of H-terminated LiH (111) and B-terminated MgB_2 (0001) surfaces, from AIMD simulations. The panels on the right provide a projection view of the LiH/MgB_2 interface highlighted in blue in the left-hand figure, along with the calculated Bader charges for selected B and Mg atoms. In these structure representations, the Li, H, B and Mg atoms are presented as large light green, small pink, small dark green and large orange spheres.

It is difficult to quantitatively correlate observed XPS binding energy shifts with an initial-state charge configuration at the photoemitting atom, especially for binding energy variations of only 1 - 2 eV and when the composition is changing. This is because the observed photoemission binding energy is not only determined by the charge state at the photoemitting atom, but also by the core-hole-induced screening response of the other electrons on the photoemitting atom (atomic relaxation) as well as by the screening response of electrons on neighboring atoms (extra-atomic relaxation). These types of core-hole screening were first described in the pioneering work of Shirley [20], are present in the XPS spectra of all solids, and are especially important in photoemission from itinerant metals [21] and oxides [22]. The difficulty can be ameliorated by comparing the XPS spectra to known standards where the local structure and composition near the photoemitting site is understood.

Aging: Near-surface Composition and Diffusion:

During our studies, we evaluated the stability of the surface and near-surface elemental compositions of the TiH_2/MgB_2 and LiH/MgB_2 samples against "aging" in the glovebox for 480 days. We believe this is one of the few studies directly examining long-term aging in a metal hydride system. Fig. 4 shows XPS data taken 480 days apart for samples stored in vials in the glovebox at nominal room temperature. The results point to the metastability and increased reactivity of the LiH/MgB_2 material.

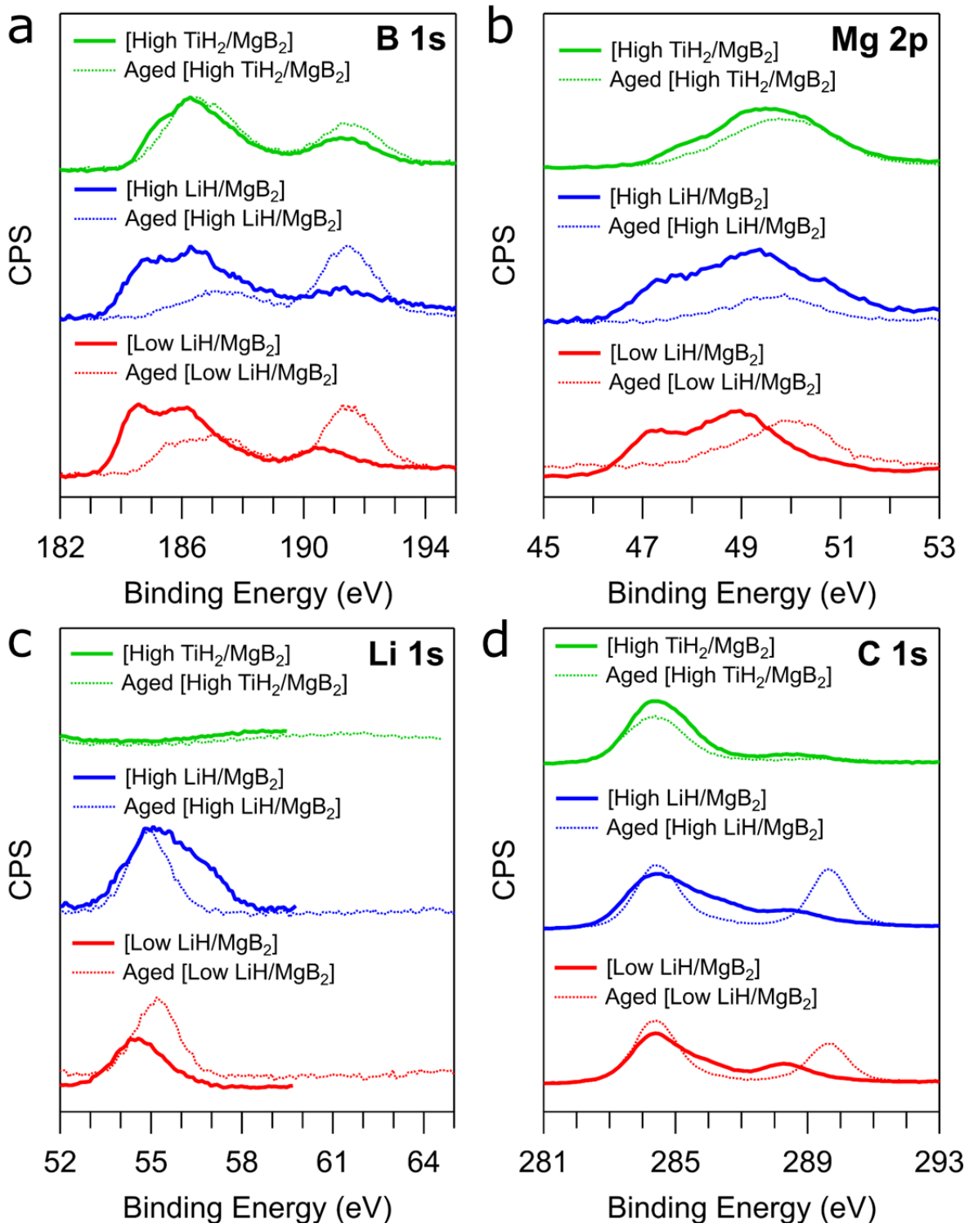

Fig. 4: XPS spectra from the [Low LiH/MgB_2] and [High LiH/MgB_2] samples, before and after ("Aged") storage in an argon glovebox for 480 days, at the (a) B 1s, (b) Mg 2p, (c) Li 1s and (d) C 1s regions. Spectra are also presented for [High TiH_2/MgB_2] as a control sample.

Looking first at the B 1s data in Fig. 4, one can see substantial changes in the [Low LiH/MgB_2] and [High LiH/MgB_2] samples with time, with only very minor changes for [High TiH_2/MgB_2] (which was similar to [Low TiH_2/MgB_2], not shown).

Table 2 quantifies these findings.

Table 2: Atomic concentrations relative to Mg determined from XPS survey spectra for samples before ("Initial") and after ("Aged") storage in an argon glovebox for 480 days.

	Initial [High TiH_2/MgB_2]	Aged [High TiH_2/MgB_2]	Aged/Initial
O/Mg	1.1	1.2	1.1
B/Mg	0.9	0.9	1.0
Ti/Mg	0.1	0.1	1.0
C/Mg	1.0	1.1	1.1
	Initial [Low LiH/MgB_2]	Aged [Low LiH/MgB_2]	Aged/Initial
O/Mg	2.2	7.7	3.5
B/Mg	1.0	1.6	1.6
Li/Mg	1.9	7.4	3.9
C/Mg	2.4	7.6	3.2
	Initial [High LiH/MgB_2]	Aged [High LiH/MgB_2]	Aged/Initial
O/Mg	4.2	7.6	1.8
B/Mg	1.0	1.5	1.5
Li/Mg	3.6	7.4	2.0
C/Mg	7.3	7.7	1.1

Here, the atomic concentrations are expressed relative to Mg, because we are unaware of any mechanisms for losing Mg from the sample under the room-temperature conditions of the sample storage, thus the Mg content should be stable. The variations seen for the "control" [High TiH_2/MgB_2] sample are as expected for a stable sample after 480 days of storage in a glovebox environment where the background contamination risk is reduced, but not zero. Relative to the presumed stable Mg, the other elements display concentration variations of ~ 10% or less for the Ti-containing sample.

In contrast, the LiH/MgB_2 samples show significant concentration variations over time. Starting with the [Low LiH/MgB_2] sample, since the Li/Mg Aged/Initial ratio increases by a factor of 3.9, far beyond any elemental increases shown by the [High TiH_2/MgB_2] control sample, Li is increasing in the surface and near-surface region over 480 days. The results from the bulk study (I) [13] suggest that it is molecular LiH that is diffusing, as undissociated LiH is detected in the bulk of the material. Lithium segregation to the surface has also been observed in prior studies of $LiBH_4$ [2]. Similarly, large increases over time are seen for O and C contamination of the

[Low LiH/MgB_2] sample. Boron is also increasing in the near-surface region, as shown by the B/Mg Aged/Initial factor of 1.6.

For [High LiH/MgB_2], time-dependent increases are also seen for Li, B, O and C, but the increases are smaller than that seen for [Low LiH/MgB_2] sample. Overall, these XPS data indicate the original LiH/MgB_2 materials are metastable and reactive in the near-surface region. Over time, LiH and B diffuse from the bulk into the near-surface region and C and O levels increase due to exposure of the reactive LiH to residual gases in the glovebox environment.

Interestingly, both aged [Low LiH/MgB_2] and [High LiH/MgB_2] possess nearly the same final values of Li/Mg, B/Mg, O/Mg and C/Mg after prolonged storage. For example, the Li/Mg ratios for the [Low LiH/MgB_2] and [High LiH/MgB_2] samples after 480 days are both 7.4. Since [Low LiH/MgB_2] initially has a Li level one-half that of [High LiH/MgB_2], Li diffusion must be faster for [Low LiH/MgB_2] because the initial Li concentration in the sample was further away from the limiting value, producing a larger driving force for diffusion. Moreover, the variations in the O and C levels are larger for [Low LiH/MgB_2] than for [High LiH/MgB_2], which is consistent with the hypothesis that the increases in O and C are caused by the presence of LiH in the surface and near-surface regions. That LiH is responsible for the increased O and C contamination over time is also evident since the [High TiH_2/MgB_2] sample, which does not contain LiH, shows relatively stable O and C levels over time.

Table 2 also shows that, over the 480 days of storage, the B/Mg levels are also changing for the LiH/MgB_2 samples compared to the [High TiH_2/MgB_2] control sample. The B/Mg Aged/Initial ratios for both [Low LiH/MgB_2] and [High LiH/MgB_2] samples increase by a factor of 1.5 – 1.6, whereas the [High TiH_2/MgB_2] sample has a constant B/Mg Aged/Initial ratio of 1.0. The mobility of B in the near surface region is therefore likely connected to the increased LiH mobility. It is possible that the presence of the LiH-B precursor interactions allow B to join LiH in the diffusion process.

Aging: Surface and Near-surface Carbonate Formation:

During our XPS studies on aging, we found that the LiH/MgB_2 materials slowly reacted with residual CO_2 in the glovebox environment to produce lithium carbonate, Li_2CO_3. The C 1s results in Fig. 4(d) show variations far beyond expectations from simple adventitious carbon contamination. Initially, before the passage of 480 days, the Low LiH/MgB_2 and High LiH/MgB_2 samples have aliphatic carbon contamination and a small amount of C contamination with carbonyl moieties at 288.4 eV. Neither sample has any carbonate contamination which would be signaled by a C 1s peak at 289.7 eV [16]. However, after 480 days in storage, a strong carbonate peak has grown in for both LiH/MgB_2 samples, a phenomenon not seen in the [High TiH_2/MgB_2] control sample (or the [Low TiH_2/MgB_2] sample, not shown). Fig. 5 shows that the carbonate contamination persists after a 90-second argon-ion etch, which indicates qualitatively that the carbonate extends into the near surface region, and is not a purely surface species. Surface carbonate contamination has been previously observed on intermetallic hydrogen storage

materials [8]. The carbonate is produced by the reaction of lithium with CO_2, a residual gas component in all argon glovebox environments [8]. In the LiH/MgB_2 samples, surface carbonate could be formed by the following reaction: $2LiH + O + CO_2 \rightarrow Li_2CO_3 + H_2$. There is enough oxygen in the near-surface region of the samples to support this chemistry.

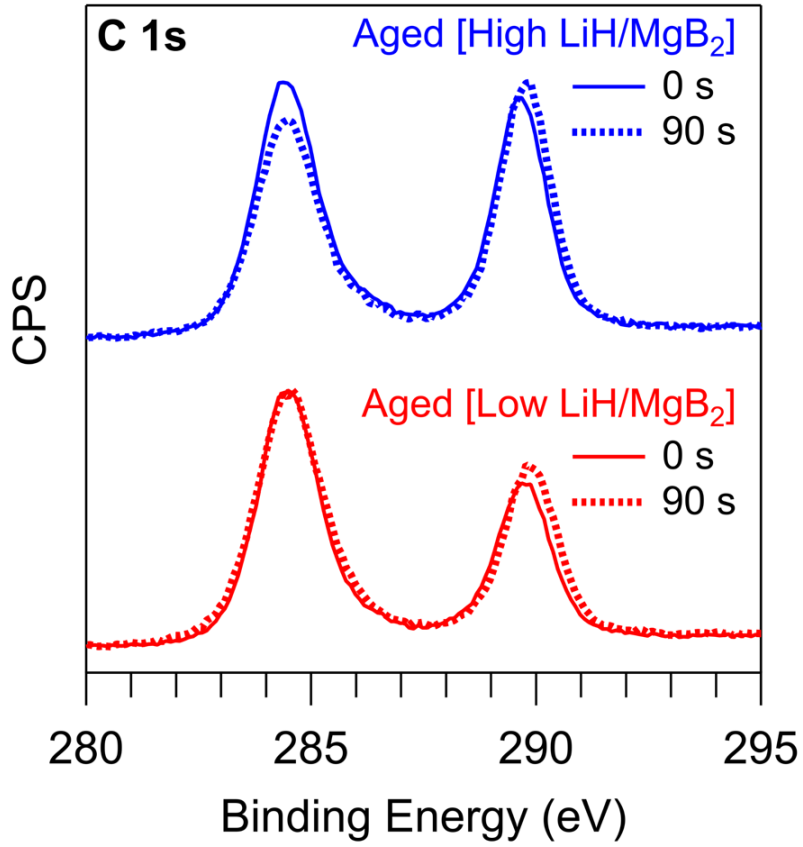

Fig. 5: Comparison of C 1s XPS spectra for zero-etch ("0 s") and 90-second argon-ion etch for Aged [Low LiH/MgB_2] and Aged [High LiH/MgB_2].

The growth of carbonate with time, coinciding with the increased near-surface LiH with time, suggests the carbonate is Li_2CO_3, growing in the near-surface region over time as these LiH/MgB_2 samples are stored.

The Li 1s XPS results shown in Fig. 4(c) confirm that the carbonate seen in Fig. 5 is Li_2CO_3. The data for [Low LiH/MgB_2] indicate that with time, there is movement in the binding energy of the Li 1s peak, from 54.5 eV to 55.1 eV, and the peak becomes more symmetrical. The data for [High LiH/MgB_2] shows that over the 480 days in storage, the Li 1s peak changes from a distribution of binding energies, asymmetric to higher BE, to a more symmetrical and uniform distribution, with binding energy 54.9 eV, very close to the 55.1 eV found for [Low LiH/MgB_2].

In other words, there was an original distribution of Li species or sites, but with time, there is a convergence to one of these species. This points to the metastability of the original LiH/MgB_2 distribution. The Li 1s binding energy that the [Low LiH/MgB_2] and [High LiH/MgB_2] samples converge to, an average binding energy 55.0 eV, agrees very well with the average literature value 54.9 for Li_2CO_3 [23, 26]. With time, Li_2CO_3 is forming on the surface and in the near-surface of the [Low LiH/MgB_2] and [High LiH/MgB_2] samples.

An important observation from Fig. 4(a) and 4(b) is that, over time, the metastable LiH-B and LiH-Mg XPS peaks marked with asterisks in Fig. 2(a) and 2(b) disappear. This can be explained by the reaction of these species with surface CO_2 to form Li_2CO_3. The results from the bulk sensitive techniques (XRD, FTIR, NMR, XAS) reported in the preceding part of the comprehensive study (I) [13] indicate no time-dependent composition variations in the bulk of the LiH/MgB_2 materials. Thus, the variations reported here reflect the surface and near-surface regions, to at least a depth of 8.4 nm but possibly deeper.

LiH/MgB_2: High-pressure Hydrogenation

The primary motivation for both this surface study and the bulk investigation of (I) [13] is to determine whether LiH and TiH_2 additives can disrupt the B-B ring structure in MgB_2, and improve the hydrogenation of MgB_2. To test this, the "Aged" samples were exposed to conditions of time, hydrogen pressure and temperature below the threshold (380 °C, 700 bar, 24 hours) hydrogenation conditions of Bulk MgB_2. The companion study (I) [13] found that [Low LiH/MgB_2] and [High LiH/MgB_2] materials do indeed hydrogenate more easily, whereas TiH_2/MgB_2 does not. The XPS results of Fig. 1 confirm in the near-surface region this bulk finding for TiH_2/MgB_2. From Fig. 1, no significant XPS lineshape variations are observed between [Low TiH_2/MgB_2] and the sample produced by HP hydrogenation, [Low TiH_2/MgB_2 HP], or between [High TiH_2/MgB_2] and [High TiH_2/MgB_2 HP], that would suggest chemical reaction. We now examine the HP hydrogenation of LiH/MgB_2 from the surface and near-surface perspectives.

Near-surface Composition Variations:

As reported in (I) [13], after HP hydrogenation for 24 hours at 700 bar and 280 ºC, the [Low LiH/MgB_2] sample had turned from a fine black powder to a uniform and hard black mass, difficult to scrape out of the vial. The [High LiH/MgB_2] sample converted into a roughly 50-50 (by volume) mixture of an off-white fluffy material on top, and a very hard black mass on the bottom of the vial. We call these two fractions "Top" and "Bottom," respectively. Our labels for the HP hydrogenation materials produced from the original [Low LiH/MgB_2] and [High LiH/MgB_2] samples are: [Low LiH/MgB_2 HP], [High LiH/MgB_2 HP Top] and [High LiH/MgB_2 HP Bottom].

Fig. 6 shows the XPS results for the [Low LiH/MgB_2] and [High LiH/MgB_2] aged samples subjected to HP hydrogenation, with the data quantified as atomic percentages relative to Mg in Table 3.

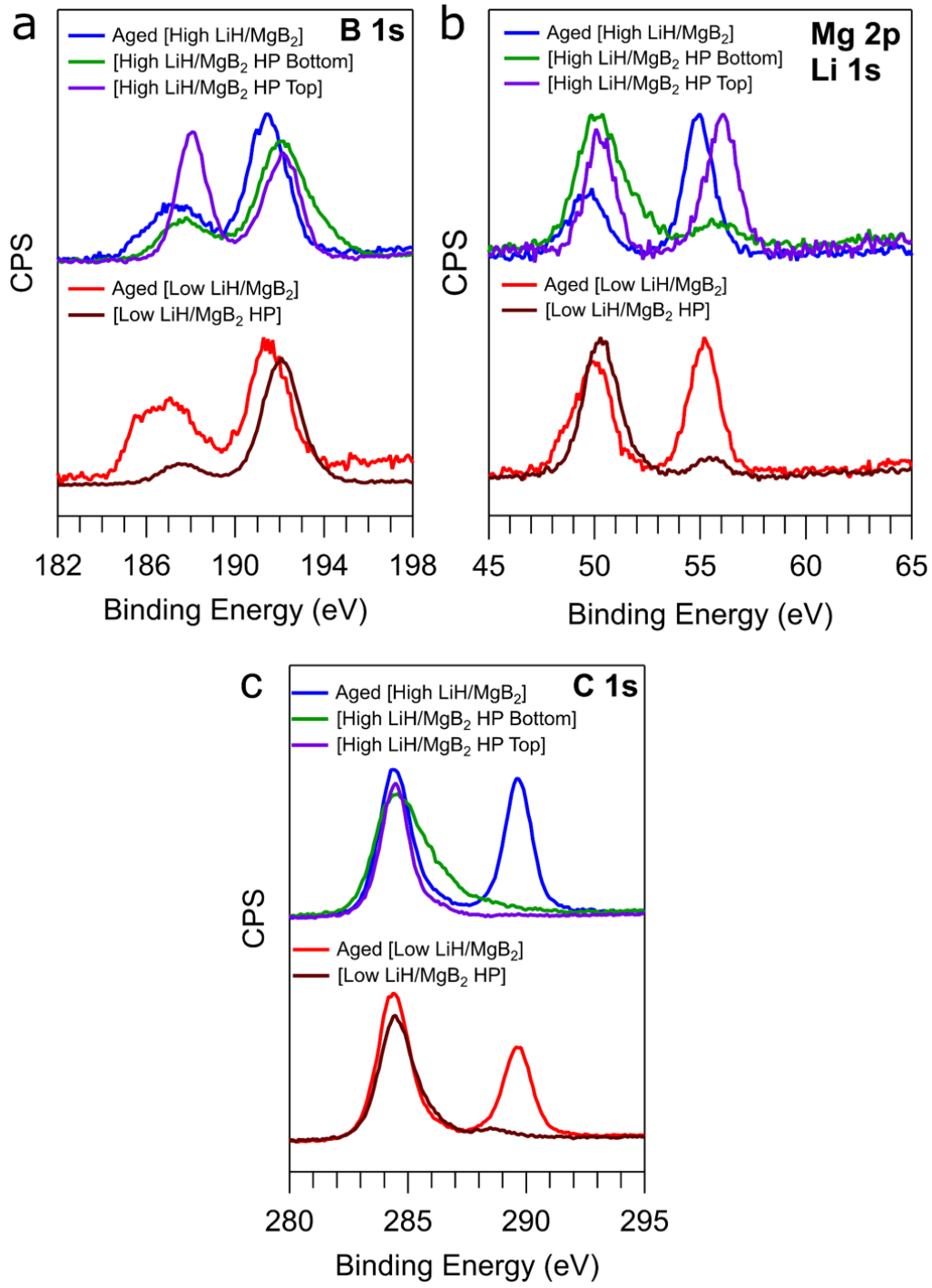

Fig. 6: XPS comparison of the [Low LiH/MgB_2] and [High LiH/MgB_2] aged samples before and after exposure to hydrogen at 700 bar and 280 °C for 24 hours. Spectra shown for the (a) B 1s, (b) Mg 2p and Li 1s and (c) C 1s regions.

Table 3: Atomic concentrations relative to Mg determined from XPS survey spectra before and after exposure to hydrogen at 700 bar and 280 °C for 24 hours.

	Aged [Low LiH/MgB_2]	[Low LiH/MgB_2 HP]	HP/Aged
O/Mg	7.7	2.4	0.3
B/Mg	1.6	1.7	1.1
Li/Mg	7.4	0.5	0.1
C/Mg	7.6	1.3	0.2
	Aged [High LiH/MgB_2]	[High LiH/MgB_2 HP Top]	HP/Aged
O/Mg	7.6	5.3	0.7
B/Mg	1.5	6.3	4.2
Li/Mg	7.4	8.2	1.1
C/Mg	7.7	5.3	0.7
	Aged [High LiH/MgB_2]	[High LiH/MgB_2 HP Bottom]	HP/Aged
O/Mg	7.6	2.8	0.4
B/Mg	1.5	2.1	1.4
Li/Mg	7.4	1.1	0.2
C/Mg	7.7	1.8	0.2

At the elevated temperature of the HP hydrogenation (280 °C) there is potential to irreversibly lose species by sublimation or desorption. This is true even though the HP reaction vessel is sealed, since deposition of volatile species on the vessel walls would still result in sample species loss. It is unlikely Mg would volatilize for the 280 °C temperature of the HP hydrogenation because the melting points [25] of possible Mg compounds, if present, are: 327 °C (MgH_2), 830 °C (MgB_2), 650 °C (Mg metal), 2852 °C (MgO) and 367 °C ($Mg(BH_4)_2$) [26]. Therefore, the atomic concentrations are again expressed as ratios to Mg, as the Mg content should be stable under the conditions of the HP experiment.

Table 3 shows that for all three of the LiH/MgB_2 samples, HP hydrogenation causes near-surface reductions in Li, C and O, but increases in B. The C 1s data in Fig. 6(c) shows that HP process eliminates carbonate from these samples, which acts to reduce both C and O via the presumed desorption of CO_2. An argon-etch analysis (not shown) showed that the near-surface region was free of carbonate as well. Since Li_2CO_3 does not sublime, the carbonate is being chemically transformed by the HP process.

The HP hydrogenation process significantly reduces the amount of lithium in the analysis region, by multiplicative factors of 0.1 for [Low LiH/MgB_2 HP] and 0.2 for [High LiH/MgB_2 Bottom].

Interestingly, for [High LiH/MgB_2 Top], there is no loss of Li but rather a slight increase (10%). The loss of Li raises suspicions of volatilization. However, the melting points [25] of possible Li compounds are: 1432 °C (Li_2O), 692 °C (LiH), 723 °C (Li_2CO_3), 268 °C ($LiBH_4$) and 367 °C ($Mg(BH_4)_2$) [26]. Except for $LiBH_4$, we don't expect these species, if produced, to be Li volatilization risks. Li metal has a very low melting point of 180.5 °C, however we find no evidence for it, via the signature Li 1s plasmon loss structure [18], in any of the LiH/MgB_2 samples of this study. $LiBH_4$ evaporation could reduce Li, but this would be accompanied by B volatilization as well. Table 3 shows there is no evidence for a loss of B as indicated by the B/Mg ratio before and after the HP exposure. To the contrary, B is enriched in these samples after HP hydrogenation.

Bardaji and co-workers [27] found that ball-milled mixtures of $xLiBH_4$ and $(1-x)Mg(BH_4)_2$, form a eutectic for $0.33 < x < 0.66$. The eutectic mixture melts at 180 °C, well below the melting points of pure $LiBH_4$ and $Mg(BH_4)_2$ and below the 280 °C of the HP hydrogenation. When the mixtures were heated further in a helium background, hydrogen desorption was detected over the temperature range 180 – 400 °C. There was no indication of significant vaporization of the eutectic mixture, which would have been detected as a major mass loss in thermogravimetric analysis experiments. Instead, hydrogen desorption was found to be the major decomposition route [27]. Thus, vaporization loss of borohydride is not expected to be significant for our experiments. Eutectic melting does explain the physical characteristics of the HP hydrogenation products and is discussed more fully in the preceding companion study (I) [13].

Hydrogenating [Low LiH/MgB_2] to [Low LiH/MgB_2 HP]:

In addition to the composition variations discussed above, other complex phenomena are observed with the HP hydrogenation. We start with hydrogenation of the [Low LiH/MgB_2] sample, showing that HP hydrogenation not only leads to borohydride production, but also induces chemical reaction between the contaminants Li_2CO_3 and boric acid.

In Fig. 6(a) we see that the HP hydrogenation to [Low LiH/MgB_2 HP] dramatically increases the intensity in the vicinity of the B 1s hydroxide-related feature, with a binding energy shift from the original 191.6 eV to 192.2 eV. This B 1s variation is accompanied by a dramatic loss of the Li_2CO_3 C 1s XPS peak in Fig. 6(c). The increased intensity for the hydroxide feature is at first puzzling, since the O/Mg ratio decreases by a factor of 0.32 when [Low LiH/MgB_2] is hydrogenated (see Table 3).

Our explanation for these changes is that during the HP hydrogenation with 700 bar hydrogen at 280 °C, Li_2CO_3 reacts with the boron-hydroxide to form lithium borate ($LiBO_2$) by the reaction: $Li_2CO_3 + 2H_3BO_3 = 2LiBO_2 + CO_2 + 3H_2O$. We presume H_3BO_3 because the B 1s XPS data in Fig. 2(a) shows the presence of hydrated boron oxide (B-OH), whose presence would only be promoted by HP hydrogenation. This known reaction [28] has the effect of reducing the overall O and C in the system via desorption of CO_2 and H_2O, explaining why the atomic fraction of O and C decrease with the HP hydrogenation. It also explains the disappearance of the Li_2CO_3

XPS peak in Fig. 6(c) with HP hydrogenation. This reaction does not, however, explain the loss of Li seen in Table 3. Lithium-deficient lithium borate glasses are reported to have a B 1s peak at 192.0 eV [29], consistent with the B 1s binding energy of 192.2 eV observed in Fig. 6(a). We note here that in (I) [13], evidence for a $LiBO_2$-like species was barely observed in the FTIR of [High LiH/MgB_2 HP Bottom], and clearly seen in the FTIR data for [High LiH/MgB_2 HP Top].

The Li 1s feature in Fig. 6(b) can in principle be produced by pure $LiBH_4$, a mixed-metal borohydride of the type $Mg_{(3-x)/2}Li_x(BH_4)_3$, a lithium borate glass, or some other Li containing species. The Li 1s envelope for [Low LiH/MgB_2 HP] in Fig. 6(b) is at 55.6 eV, intermediate between the 56.0 eV Li 1s binding energy for pure $LiBH_4$ [2,4] and the 55.3 eV observed for Li-deficient borate glass [31]. The observation of borohydride would be consistent with the bulk studies in (I) [13], which showed the formation of mixed-metal (Li/Mg) borohydride phases for [Low LiH/MgB_2 HP], although it is unknown if Li 1s XPS can distinguish between pure $LiBH_4$ and $Mg_{(3-x)/2}Li_x(BH_4)_3$.

Turning to the boride region shown in Fig. 6(a), we see that the B 1s spectral envelope for [Low LiH/MgB_2] becomes sharper and moves to higher binding energy at 187.6 eV with HP hydrogenation, producing [Low LiH/MgB_2 HP]. This binding energy shift is consistent with the production of borohydride. We are unaware of literature XPS results for $Mg(BH_4)_2$. However, the literature value for the B 1s peak of $LiBH_4$ is 187.9 eV [2] when corrected with our C 1s calibration. If a similar B 1s binding energy prevailed for $Mg_{(3-x)/2}Li_x(BH_4)_3$, then the XPS data would be consistent with the bulk study of (I) [13], which found mixed-metal borohydride production during the HP hydrogenation of [Low LiH/MgB_2].

Hydrogenating [High LiH/MgB_2] to [High LiH/MgB_2 Bottom] and [High LiH/MgB_2 Top]:

Recall that HP hydrogenation of the [High LiH/MgB_2] sample created a two-phase product [High LiH/MgB_2 HP Bottom] and [High LiH/MgB_2 HP Top], which were recovered and analyzed separately. Here we discuss the XPS results that clarify the nature of these two products created by the HP hydrogenation.

The "hydroxide" B1s peak for both [High LiH/MgB_2 HP Bottom] and [High LiH/MgB_2 HP Top] appear at 192.2 eV, as was seen for [Low LiH/MgB_2 HP], suggesting formation of a lithium-deficient borate glass, produced by the reaction of Li_2CO_3 with boron hydroxide. This reaction explains the disappearance of the C 1s carbonate feature for [High LiH/MgB_2 HP Bottom] and [High LiH/MgB_2 HP Top] seen in Fig. 6(c).

Turning attention to the boride region in Fig. 6(a), we see that HP hydrogenation produces a shift to higher binding energy, from the original 187.3 eV for [High LiH/MgB_2] up to 187.8 eV for [High LiH/MgB_2 HP Bottom] and eventually to 188.0 eV for [High LiH/MgB_2 HP Top]. These are close to the B 1s XPS binding energy observed for $LiBH_4$, 187.9 eV [2]. The production of borohydride in the [High LiH/MgB_2 HP Bottom] and [High LiH/MgB_2 HP Top] samples is in

line with the bulk observations of the HP hydrogenation reported in (I) [13] where a mixed-metal borohydride of the type $Mg_{(3-x)/2}Li_x(BH_4)_3$ was found.

With HP hydrogenation, the Li 1s peak in Fig. 6(b) moves to higher binding energy, reaching 55.9 eV for [High LiH/MgB_2 HP Bottom] and 56.0 eV for [High LiH/MgB_2 HP Top], in the direction of the 56.6 eV binding energy reported for Li 1s from clean $LiBH_4$ [2]. This indicates a larger borohydride fraction produced in the High LiH/MgB_2 hydrogenation than in the Low LiH/MgB_2 hydrogenation, consistent with the bulk observations reported in (I) [13].

The creation of a glassy lithium borate melt at the 280 °C temperature explains the macroscopic physical change observed for the samples upon HP hydrogenation. The [Low LiH/MgB_2 HP] material was rock-hard, which is consistent with the creation of a glassy melt at the interfaces of the particles during the HP hydrogenation, fusing them together. The same hardening phenomenon was seen for [High LiH/MgB_2 HP Bottom].

LiH/MgB_2: Desorption

The samples resulting from the HP Hydrogenation were subjected to a thermal desorption ramp (3 °C/minute) to 380 °C in a Sieverts apparatus into a static vacuum. Due to limited sample yields, XPS data were collected only for desorption from the [Low LiH/MgB_2 HP] and [High LiH/MgB_2 HP Bottom] samples that produced the desorbed samples [Low LiH/MgB_2 HPD] and [High LiH/MgB_2 HPD Bottom], respectively. There were no TiH_2/MgB_2 control samples for this comparison, as a thermal desorption study was not conducted for [Low TiH_2/MgB_2] and [High TiH_2/MgB_2] because they did not adsorb hydrogen in the HP hydrogenation experiment.

XPS results from the desorbed samples are shown in Fig. 7 with the atomic concentrations relative to Mg quantified in Table 4. The results show that the LiH/MgB_2 materials are not reversible, since desorption of the hydrogenated samples do not return the system to the original LiH/MgB_2 state, in agreement with the bulk findings of (I). In addition, Li-deficient borate glass is removed by the thermal desorption process.

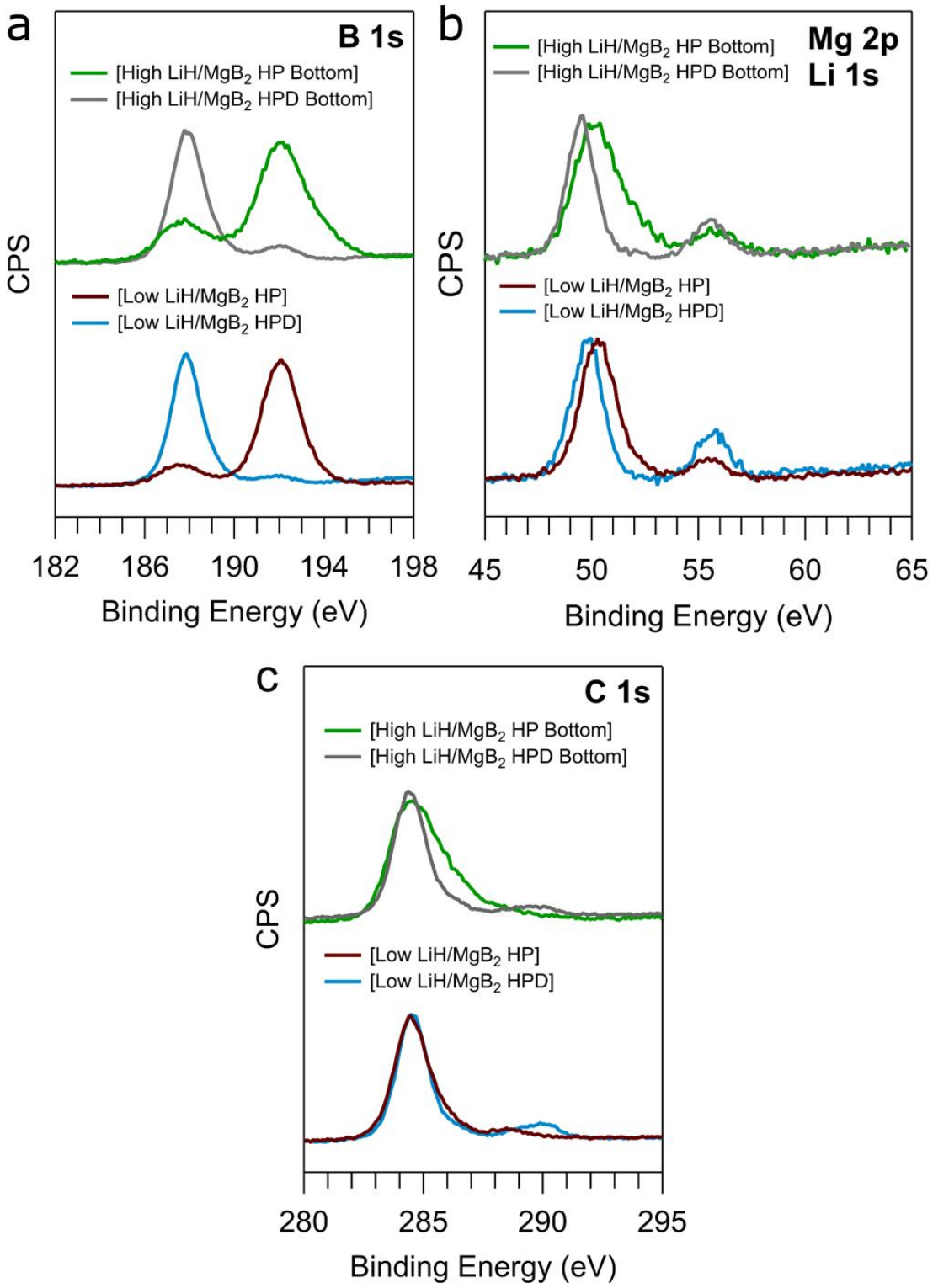

Fig. 7: XPS comparison of [Low LiH/MgB_2 HP] and [High LiH/MgB_2 HP] before desorption and [Low LiH/MgB_2 HPD] and [High LiH/MgB_2 HPD Bottom] after desorption at 380 °C into static vacuum with a temperature ramp of 3 °C/minute. Core-level spectra measured at the (a) B 1s, (b) Mg 2p and Li 1s. and (c) C 1s regions.

Table 4: Atomic concentrations relative to Mg determined from XPS survey spectra for [Low LiH/MgB_2 HP] and [High LiH/MgB_2 HP Bottom] before desorption and [Low LiH/MgB_2 HPD] and [High LiH/MgB_2 HPD Bottom] after desorption at 380 °C.

	[Low LiH/MgB_2 HP]	[Low LiH/MgB_2 HPD]	HPD/HP
O/Mg	2.4	2.2	0.9
B/Mg	1.7	4.0	2.4
Li/Mg	0.5	1.7	3.4
C/Mg	1.3	3.6	2.8
	[High LiH/MgB_2 HP Bottom]	[High LiH/MgB_2 HPD Bottom]	HPD/HP
O/Mg	2.8	2.2	0.8
B/Mg	2.1	3.8	1.8
Li/Mg	1.1	1.5	1.3
C/Mg	1.8	2.8	1.5

The most dramatic aspect of the B1s XPS data in Fig. 7(a) is the great reduction in prominence of the Li-deficient borate glass feature at 192.2 eV for both [Low LiH/MgB_2 HPD] and [High LiH/MgB_2 HPD Bot]. The maximum temperature of the desorption, 380 °C, is well below the melting point of lithium borate glasses, although it is above the glass transition temperature for Li-deficient borate glasses [31]. The increased levels of Li in the near-surface regions for both [Low LiH/MgB_2 HPD] and [High LiH/MgB_2 HPD Bottom] in Table 4 suggest sublimation of the Li-deficient borate glass is unlikely. One could argue that the loss of borate is due to its creation near the surface due to the reaction of Li with environmental CO_2, and therefore, it exists mostly in the near surface regions. When heated, the Li-deficient glass constituents then diffuse into the bulk, depleting the near-surface region probed by XPS. Again, the increased levels of Li in Table 4 argue against diffusion as the reason for the reduced prominence of the Li-deficient borate glass feature at 192.2 eV. Nonetheless, FTIR data reported in (I) [13] indicated that when desorbed, the borate leaves the sample.

Another possibility is that the glass is heavily hydroxylated, and desorption of water during the heating to 380 °C removes the oxidized B 1s XPS feature by removing oxygen bound to B, leaving unoxidized and presumably elemental B. Fig. 7(a) reports that desorption leading to samples [Low LiH/MgB_2 HPD] and [High LiH/MgB_2 HPD Bottom] produces the same B 1s peak at 187.9 eV binding energy. This peak corresponds to elemental B [1, 32, 33], supporting the elimination of hydroxylated borate glass by desorption of water.

Fig. 7(b) shows that after desorption, the Mg 2p binding energy for [Low LiH/MgB_2 HPD] is 49.9 eV, which is close to the reported binding energy for MgH_2 of 50.0 eV after correction to our C 1s standard [34]. However, the desorption temperature was high enough such that MgH_2, if formed, would desorb hydrogen to produced Mg metal. Thus, we assign the peak at 49.9 eV to

Mg metal. The Mg 2p binding energy for [High LiH/MgB_2 HPD Bottom] is 49.5 eV. This compares well with the binding energy reported previously for clean Mg metal, 49.6 [35] after correction to our C 1s calibration standard. Mg metal was found in the XRD of both [Low LiH/MgB_2 HPD] and [High LiH/MgB_2 HPD Bottom] as reported in (I) [13].

The binding energy of the Li 1s after desorption for [Low LiH/MgB_2 HPD] and [High LiH/MgB_2 HPD Bottom] are 55.7 eV and 55.6 eV, respectively. These do not correspond to oxides or carbonate, since the literature reports (on average) the Li 1s binding energies of Li_2O, LiOH and Li_2CO_3 are 53.2 eV, 54.1 eV and 54.9 eV, respectively [23, 24]. Rather, it seems to correspond to LiB_2 for which the reported literature Li 1s binding energy is 55.7 eV, when correcting for our C 1s calibration [31].

Fig. 8 brings together in one figure the lineshape variations for the Low LiH/MgB_2 and High LiH/MgB_2 samples through the full cycle of hydrogenation and desorption which have been discussed in detail separately above.

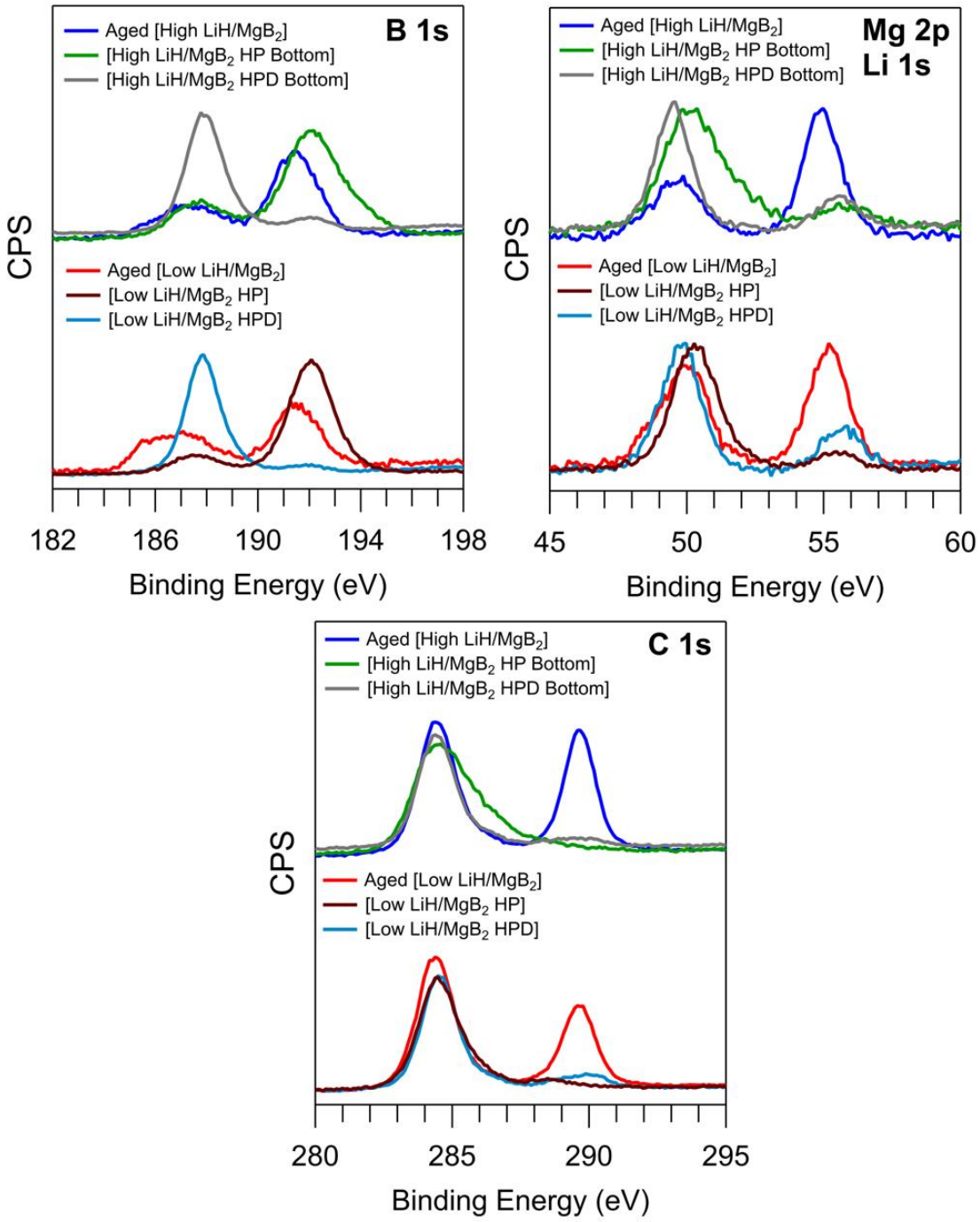

Fig. 8: XPS comparison at the (a) B1s region, (b) Mg 2p and Li 1s region and (c) for the C 1s region for [Low LiH/MgB_2] and [High LiH/MgB_2] samples: "as prepared" with 480 days of glovebox storage, after exposure to hydrogen at 700 bar and 280 °C for 24 hours, and after desorption into static vacuum up to 380 °C.

Conclusions

The studies of the bulk properties of LiH/MgB_2 reported in (I) showed no indication of time-dependent variations in elemental concentrations, species stability or chemistry for a given material state in the sequence material synthesis → hydrogenation → dehydrogenation. In contrast, the XPS studies of the LiH/MgB_2 system show a dynamic environment within the first ~10 nm of the material surface.

Introducing LiH to MgB_2 creates metastable LiH-B and LiH-Mg states that render the material much more reactive to ambient oxygen (O_2, H_2O) and carbon contamination, and very importantly, to ambient CO_2 as the material is stored for prolonged times in a glovebox environment. The combination of LiH and CO_2 leads to the formation of Li_2CO_3 in the surface and near surface regions. In addition, over time, a substantial enrichment of both LiH and B takes place in the near-surface regions, with the diffusion driven by concentration gradients, which stabilize to the same values of concentration regardless of the starting initial concentrations.

The addition of LiH significantly improves the hydrogenation of MgB_2. With exposure to hydrogen at 200 bar and 280 ºC for 24 hours, borohydride is formed in the near-surface regions at temperatures 100 ºC below the threshold for hydrogenation of Bulk MgB_2 for the same conditions of pressure and time. The more LiH is added, the greater the production of borohydride. A side effect of the initial hydrogenation was that the conditions cause near-surface Li_2CO_3 contamination to react with boron hydroxide in the sample to form a Li-deficient glassy lithium borate melt at the interfaces of the particles, fusing them together in the [Low LiH/MgB_2 HP] and [High LiH/MgB_2 HP Bottom] samples.

The addition of LiH also improved hydrogen desorption from the borohydride. Heating the hydrogenated samples to 380 ºC reduced near-surface levels of O, increased near-surface levels of C, Li and B, and leads to the near-disappearance of the Li-deficient glassy lithium borate. XPS analysis of the desorbed products shows the material is not reversible, because desorption does not lead back to LiH/MgB_2, but rather produces elemental B and in some cases, Mg metal. In contrast to LiH, TiH_2 does not react with MgB_2. Furthermore, high pressure hydrogenation yields only unreacted TiH_2 and MgB_2 in the surface and near-surface regions.

Future work will focus on a better understanding of the precursor LiH-B and LiH-Mg states and the reaction that is taking place between LiH and MgB_2 during the hydrogenation. A future publication will present the results of the AIMD investigation of the LiH/MgB_2 material system.

Finally, we note here that the near-surface phenomena observed here, namely the production and evolution of metastable LiH-B and LiH-Mg species, their increased reactivity, the time-dependent changes in Li and B concentration caused by diffusion and their reactivity towards hydrogen and ambient gases (CO_2) will be especially important for future studies where LiH

additive is introduced into nanoscale or nanoconfined complex metal hydride systems [36, 37] involving B, Mg, MgH_2, or MgB_2.

Acknowledgements

The authors acknowledge financial support through the Hydrogen Storage Materials Advanced Research Consortium (HyMARC) of the U.S. Department of Energy (DOE), Office of Energy Efficiency and Renewable Energy, Fuel Cell Technologies Office under Contracts DE-AC52-07NA27344 and DE-AC04-94AL85000. Part of the work was performed under the auspices of the DOE by Lawrence Livermore National Laboratory under Contract DE-AC52-07NA27344. Sandia National Laboratories is a multi-mission laboratory managed by National Technology and Engineering Solutions of Sandia, LLC, a wholly owned subsidiary of Honeywell International Inc., for the DOE's National Nuclear Security Administration under contract DE-NA0003525. Portions of this research were performed on BLs 6.3.1.2 and 8.0.1.1 at the Advanced Light Source, Lawrence Berkeley National Laboratory, which is supported by the Director, Office of Science, Office of Basic Energy Sciences, of the U.S. DOE under Contract DE-AC02–05CH11231. XPS work at the Molecular Foundry of the Lawrence Berkeley National Laboratory was supported by the Office of Science, Office of Basic Energy Sciences, of the U.S. Department of Energy under Contract No. DE-AC02-05CH11231. Thanks are extended to Ted Schoeck for illuminating conversations.

References:

1. Liu, Y. S.; Klebanoff, L. E.; Wijeratne, P.; Cowgill, D. F.; Stavila, V.; Heo, T. W.; Kang, S.; Baker, A. A.; Lee, J. R. I.; Mattox, T. M.; Ray, K. G.; Sugar, J. D.; Wood, B. C.; *"Investigating Possible Kinetic Limitations to MgB_2 Hydrogenation," Int. J. Hydrogen Energy* **2019**, *44* (59), 31239–31256.

2. Kato, S.; Bielmann, M.; Borgschulte, A.; Zakaznoya-Herzog, V.; Remhof, A.; Orimo, S.-I.; Zuttel, A., *"Effect of Surface Oxidation of $LiBH_4$ on the Hydrogen Desorption Mechanism,"* Phys. Chem. Chem. Phys. **12** (2010) 10950-10955.

3. Chen, J.; Kuriyama, N.; Xu, Q.; Takeshita, T.; Sakai, T.; *Reversible Hydrogen Storage via Titanium-catalyzed $LiAlH_4$ and Li_3AlH_6,"* J. Phys. Chem. B **105** (2001) 11214-11220.

4. Deprez, E.; Muñoz-Márquez, M.A.; Jimenez de Haro, M.C.; Palomares, F.J.; Soria, F.; Dornheim, M.; Bormann, R.; Fernández , A.*; "Combined X-ray Photoelectron Spectroscopy and Scanning Electron Microscopy Studies of the $LiBH_4$-MgH_2 Reactive Hydride Composite with and without a Ti-based Additive,"* J. Appl. Phys. **109**, (2011) 014913 1-10.

5. Reyhani, A.; Mortazavi, S.Z.; Mirershadi, S.; Moshfegh, A.Z.; Parvin, P.; and Nozad Golikand, A.; *"Hydrogen Storage in Decorated Multiwalled Carbon Nanotubes by Ca, Co, Fe, Ni, and Pd Nanoparticles under Ambient Conditions,"* J. Phys. Chem. C **115** (2011) 6994–7001.

6. Christian, M.L.; and Aguey-Zinsou, K.-F.; *"Core-Shell Strategy Leading to High Reversible Hydrogen Storage Capacity for $NaBH_4$,"* ACS Nano, **6** (2012) 7739 – 7751.

7. Huang, C.-C.; Chen, Chen, H.-M.; Chen, C.-H.; Huang, J.-C., *"Effect of Surface Oxides on Hydrogen Storage of Activated Carbon,"* Separation and Purification Technology **70** (2010) 291–295.

8. Selvman, P.; Viswanathan, B.; Srinivasan, V., *"Evidence for the Formation of Surface Carbonates on Some Hydrogen Storage Intermetallic Compounds: An XPS Study,"* Int. J. Hydrogen Energy **15** (1990) 133-137.

9. Yang, J., Fu, H., Song, P., Zheng, J. and Li, X., *"Reversible Dehydrogenation of $Mg(BH_4)_2$-LiH Composite Under Moderate Conditions,"* Int. J. Hydrogen Energy **37** (2012) 6776 – 6783.

10. Grube, E., Jensen, S.R.H., Nielsen, U.G., and Jensen, T.R. *"Reactivity of Magnesium Borohydride-Metal Hydride Composites, γ-$Mg(BH_4)_2$-MH_x, M = Li, Na, Mg, Ca,"* J. Alloys and Compounds **770** (2019) 1155 – 1163.

11. Puszkiel, J., Gasnier, A., Amica, G., and Gennari, F., *"Tuning $LiBH_4$ for Hydrogen Storage: Destabilization, Additive, and Nanoconfinement Approaches,"* Molecules **25** (2020) 163.

12. Siegel, D.J., Wolverton, C. and Ozolins, V., *"Thermodynamic Guidelines for the Prediction of Hydrogen Storage Reactions and Their Application to Destabilized Hydride Mixtures,"* Phys. Rev. B **76**, 134102 (2007).

13. J.L. Snider, Y.-S. Liu, A.M. Sawvel, L.F. Wan, V. Stavila, T.M. Mattox et al. "The Influence of LiH and TiH_2 on Hydrogen Storage in MgB_2 I: Promotion of Bulk Hydrogenation at Reduced Temperature," International Journal of Hydrogen Energy **XX** (2021) yyy – zzz.

14. Seah, M.P.; Dench, W.A. Dench; *"Quantitative Electron Spectroscopy of Surfaces: A Standard Data Base for Electron Inelastic Mean Free Paths in Solids,"* Surface and Interface Anal. **1**, (1979) 2 – 11.

15. Standard enthalpies of formation for TiH_2, MgB_2, TiB_2 and MgH_2 required as input to calculate $\Delta H_{f,rxn}$ were taken from the NIST Chemistry Webbook: https://webbook.nist.gov/chemistry/

16. Liu, Y.-S.; Ray, K.G.; Jørgensen, M.; Mattox, T.M.; Cowgill, D.F.; Eshelman, H.V.; Sawvel, A.M.; Snider, J.L.; York, W.; Wijeratne, P.; Pham, A.M.; Gunda, H.; Li, S.; Heo, T.W.; Kang, S. Jensen, T.R., Stavila, V.; Wood, B.C.; and Klebanoff, L.E.; *"Nanoscale Mg-B Via Surfactant Ball Milling of MgB_2: Morphology, Composition and Improved Hydrogen Storage Properties"* J. Phys. Chem. C **124** (2020) 21761-21771.

17. Aswal, D.K.; Muthe, K.P.; Singh, A.; Sen, S.; Shah, K.; Gupta, L.C.; Gupta, S.K.; Sahni, V.C.; *"Degradation Behavior of MgB_2 Superconductor*," Physica C **363** (2001) 208-214.

18. Kowalczyk, S.P.; Ley, L. McFeely, F.R.; Pollak, R.A.; and Shirley, D.A.; *"X-ray Photoemission from Sodium and Lithium,"* Phys. Rev. B **8** (1973) 3583 – 3585.

19. K.G. Ray, private communication to L.E. Klebanoff, December 28, 2020.

20. Shirley, D.A.; *"The Effect of Atomic and Extra-Atomic Relaxation on Atomic Binding Energies,"* Chem. Phys. Lett. **16** (1972) 220 - 225.

21. See, A.K.; Klebanoff, L.E., *"Nature of Extra-Atomic Core-Hole Screening in Ferromagnetic Ni,"* Phys. Rev. Lett. **74** (1995) 1454 – 1457.

22. Vasquez, R.P., "X-ray Photoemission Study of MgB_2," Phys. Rev. B **64** (2001) 052510 1-4.

23. Kozen, A.C.; Pearse, A.J.; Lin, C.-F.; Schroeder, M.A.; Noked, M.; Lee, S.B.; Rubloff, G.W.; *"Atomic Layer Deposition and in Situ Characterization of Ultraclean Lithium Oxide and Lithium Hydroxide,"* J. Phys. Chem. C **118** (2014) 27749−27753.

24. Yao, K.P.C.; Kwabi, D.G.; Quinlan, R.A.; Mansour, A.N.; Grimaud, A.; Lee, Y.-L., Lu, Y.-C.; Shao-Horn, Y.; *"Thermal Stability of Li_2O_2 and Li_2O for Li-Air Batteries: In Situ XRD and XPS Studies,"* J. Electochem. Soc. **160** (2013) A824 – A831.

25. Melting points of materials provided by: CRC Handbook of Chemistry and Physics, 57th Edition, CRC Press, 1976.

26. White, J.L.; Strange, N.A.; Sugar, J.D.; Snider, J.L.; Schneemann, A.; Lipton, A.S.; Toney, M.F.; Allendorf, M.D.; Stavila, V.; *"Melting of Magnesium Borohydride under High Hydrogen Pressure: Thermodynamic Stability and Effects of Nanoconfinement,"* Chem. Mater. **32** (2020), 5604–5615.

27. E.G. Bardaji, Z. Zhao-Karger, N. Boucharat, A. Nale, M.J. van Setten, W. Lohstroh, E. Röhm, M. Catti and M. Fichtner, "$LiBH_4$-$Mg(BH_4)_2$: A Physical Mixture of Metal Borohydrides as Hydrogen Storage Material," J. Phys. Chem. C **115** (2011) 6095 – 6101.

28. Roman-Tejeda, A.; Pfeiffer, H.; *"α→γ Lithium Borate Phase Transition Produced During the CO_2 Chemisorption Process,"* Therm. Anal. Calorim. **110** (2012) 807–811.

29. Chowdari, B.V.R.; Rong, Z. *"Study of the Fluorinated Lithium Borate Glasses,"* Solid State Ionics **78** (1995) 133-142.

30. Serebryakova, T.I., Lyashenko, V.I., and Levandovskii, V.D., *"Interaction in the System Li-B and Some Properties of Lithium Boride Phases,"* Powder Metallurgy and Metal Ceramics **33** (1994) 49 – 53.

31. Martin, S.W.; Angell, C.A.; *"Glass Formation and Transition Temperatures in Sodium and Lithium Borate and Aluminoborate Melts Up to 72 Mol % Alkali,"* J. Non-crystalline Solids **66** (1984) 429-442.

32. Foo, W.C.; Ozcomert, J.S.; Trenary, M.; *"The Oxidation of the β-rhombohedral boron (111) Surface,"* Surf. Sci. **255** (1991) 245-258.

33. Ong, C.W.; Huang, H.; Zheng, B.; Kwok, R.W.M.; Hui, Y.Y.; Lau, W. M.; *"X-ray Photoemission Spectroscopy of Nonmetallic Materials: Electronic Structures of Boron and B_xO_y"* J. Appl. Phys. **95** (2004) 3527 - 3534.

34. He, Z.X.; Pong, W.; "X-ray Photoelectron Spectra of MgH_2," Phys. Scr. **41** (1990) 930 – 932.

35. Chen, C.; Splinter, S.J.; Do, T.; McIntyre, N.S.; "Measurement of Oxide Film Growth on Mg and Al Surfaces Over Extended Periods Using XPS," Surf. Sci. **382** (1997) L652 – L657.

36. A. Schneemann, J.L. White, S. Kang, S. Jeong, L.F. Wan, E.S. Cho, T.W. Heo, D. Prendergast, J.J. Urban, B.C. Wood, M.D. Allendorf and V. Stavila, *"Nanostructured Metal Hydrides for Hydrogen Storage,"* Chem. Rev. **118** (2018) 10775 – 10839.

37. V. Stavila, L.E. Klebanoff, J.J. Vajo and P. Chen, “Development of On-board Reversible Complex Metal Hydrides for Hydrogen Storage,” Chapter 6 in “*Hydrogen Storage Technology, Materials and Applications*, Ed. L.E. Klebanoff, (Taylor and Francis, Boca Raton, 2012), p. 133.